Dissociative Ligand Exchange at Identical Molecular and Carbon Nanoparticle Binding Sites

Dissociative ligand exchange at identical molecular and carbon nanoparticle binding sites

Corey J. Kaminsky,[†ø] Sterling B. Chu,[†ø] Richard I. Sayler,[‡] Seokjoon Oh,[†] Patrick W. Smith,[†] Joshua Wright,[‖§] R. David Britt,[‡] and Yogesh Surendranath[†*]

[†]Department of Chemistry, Massachusetts Institute of Technology, Cambridge, Massachusetts 02139, United States

[‡]Department of Chemistry, University of California at Davis, Davis, California 95616, United States

[‖]Advanced Photon Source, Argonne National Laboratory, 9700 Cass Avenue, Lemont, Illinois 60439, United States

[§]Illinois Institute of Technology, 3300 South Federal Street, Chicago, Illinois 60616, United States

Supporting Information Placeholder

ABSTRACT: Ligand exchange reactions at nanoparticle surfaces are critical to the formation and function of nanomaterials. The kinetics of surface ligand exchange derive from a combination of factors related to local binding site structure and the surface reaction environment. Here, we isolate the contributions of the surface reaction environment by comparing the ligand exchange kinetics of a carbon nanoparticle binding site to that of a molecular analog with identical binding site structure. Specifically, we synthesize a graphite-conjugated pseudo-octahedral ruthenium complex, GCC-Ru, bearing a single exchangeable phosphine ligand and compare its kinetics of ligand exchange to that of the identical molecular Ru complex. Using a combination of spectroscopies, we establish common molecular coordination environments and oxidation states for GCC-Ru and the molecular analog and use ^{19}F-NMR to interrogate the kinetics and mechanism of ligand exchange. We find that surface conjugation results in a two- to three-fold rate enhancement which derives from compensating changes to $\Delta H^{\ddagger}$ and $\Delta S^{\ddagger}$ for a common dissociative mechanistic pathway. Based on these data, we develop a model that explains these changes to the activation parameters through charge screening by the carbon and its impact on the local solvent environment at the surface binding site. This work highlights the key role of the solvent environment at a conductive surface in facilitating ligand exchange reactions.

Introduction

Ligand exchange reactions on the surfaces of nanomaterials are critical elementary steps in thermal and electrochemical heterogeneous catalysis[1-3] and are essential for controlling the growth,[4-6] morphology[7-9] and photoluminescent properties[10-15] of nanoparticles.[16-18] However, molecular-level insights into surface ligand exchange reactions on nanomaterials are limited for the following reasons: First, the structure of each surface binding site is often unknown and there invariably exists a multitude of different ligand binding sites with varying local coordination environments and electronic structures.[19-28] Second, ligand exchange at nanomaterials is strongly influenced by the secondary environment beyond the binding site itself. In particular, ligand exchange reactions on nanoparticles display strong dependence on lateral interactions with adjacent ligands,[29,30] the charge state of the surface,[17] the size of the nanoparticle core,[27,30-32] the identity of the solvent,[33] and the presence of other (un)bound ligands which can promote exchange.[24-26,34,35] The centrality of ligand exchange reactions for the formation, manipulation and the ultimate reactivity of nanoparticle surfaces motivates the development of precise strategies for disentangling the contributions from the local structure and environment on the kinetics of surface ligand exchange reactions.

In principle, one could disentangle the local structure and environmental effects for surface ligand exchange reactions if one could compare the reactivity of the surface site to that of a discrete molecular species of identical local structure. Unfortunately, for most materials, it is difficult, if not impossible to construct a molecular site that faithfully reproduces the local structures of the binding sites on extended solids (Figure 1, top).[36] In this respect, an alternative paradigm is to link a molecularly well-defined surface site for ligand exchange onto an otherwise inert nanomaterial and compare its ligand exchange reactivity to that of a discrete molecular analog of identical local structure (Figure 1, bottom). The success of this strategy depends critically on the nature of the linkage. For linkages that provide negligible electronic interaction between the solid and the appended sites, the environment of the appended site is expected to be distinct from that of the surface. Instead, understanding surface ligand exchange using a bottom-up approach requires a strategy for integrating the appended site *into* the surface.

We have shown that discrete molecules can be incorporated into carbon surfaces through linkages that confer strong electronic coupling with the solid. Specifically, we demonstrated that conjugating molecular active sites to graphitic carbon surfaces through pyrazine linkages affords a high degree of electronic communication between the molecular site and the carbon host.[37,38] We refer to these materials collectively as graphite-conjugated catalysts (GCCs).[37-43] We have shown that the electronic coupling afforded by this linkage makes the molecular site behave as part of the material, rather than merely appended to it.[37-43] We envisioned that this platform would be an ideal model system for rigorously isolating the role of the surface reaction environment in contributing to the kinetics of surface ligand exchange.

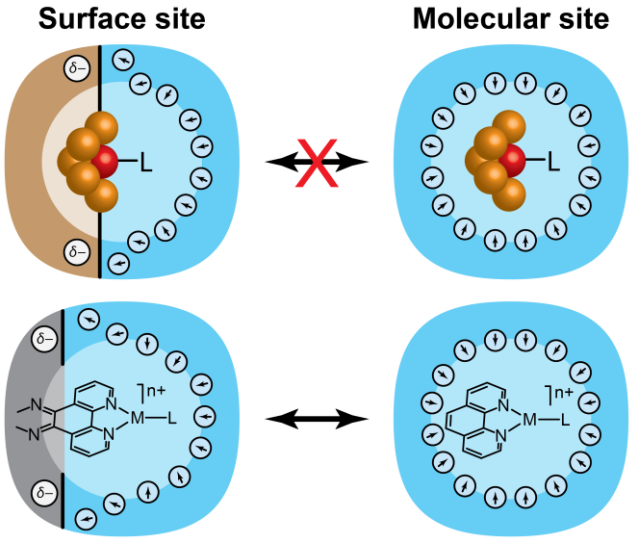

Figure 1. Top: Simplified cartoon of nanoparticle ligand (L) binding site and the inaccessible molecular analog of identical structure. Bottom: Simplified cartoon of a graphite-conjugated heterogeneous binding site and the corresponding molecular analog of identical structure that is synthetically accessible.

Leveraging the unique behavior of GCCs, we sought to isolate the role of the surface environment in impacting the activation metrics for a simple dissociative ligand exchange reaction. Herein, we synthesize a graphite-conjugated pseudo-octahedral ruthenium complex bearing a single exchangeable phosphine ligand and compare its kinetics of ligand exchange to that of the identical molecular Ru complex. We establish common molecular coordination environments and oxidation states for the GCC and molecular analog and use ^{19}F-NMR to interrogate the kinetics and mechanism of ligand exchange. We demonstrate that heterogenization results in a two- to three-fold rate enhancement which derives from compensating changes to $\Delta H^{\ddagger}$ and $\Delta S^{\ddagger}$. Finally, we present a model that rationalizes these changes to the activation parameters through charge screening by the support and its impact on the local solvent environment at the surface.

Results and Discussion.

Synthesis and characterization

The soluble complex and the diamine surface functionalization precursors were synthesized by treating a solution of [Cp(η^6-naph)Ru](PF_6) (naph = naphthalene) in dimethylformamide with tris(*p*-fluorophenyl)phosphine (PAr^{F}_3) and the corresponding bis(imine) ligand (dipyrido[3,2-*a*:2′,3′-*c*]phenazine (dppz) or 5,6-diamino-1,10-phenanthroline (phenda)). The product complexes, [CpRu(dppz)PAr^{F}_3]$^+$ and [CpRu(phenda)PAr^{F}_3]$^+$, were cleanly isolated from these mixtures as the PF_6^- salts (Scheme 1a, see Supplemental Information (SI) for details). To access the graphite-conjugated species, high surface area carbon powder or pre-anodized glassy carbon plates were treated with [CpRu(phenda)PAr^{F}_3]$^+$ in DMSO at 60 °C (Scheme 1b, See SI for details). The resulting material is referred to as GCC-Ru. In general, we have found that the surface functionalization chemistry proceeds similarly on both the anodized glassy carbon electrodes and high surface area Monarch carbon powders.[41] The former provide access to facile characterization by XPS and electrochemistry whereas the latter provides a high volumetric density of active sites ideally suited to XAS characterization and quantitative ligand exchange kinetic studies.

The high surface area carbon powder GCC-Ru samples used for ligand exchange studies consists of carbon nanoparticles. Transmission electron microscopy (TEM) reveals that GCC-Ru consists of ~20 nm particles that aggregate under the TEM conditions (Figure S1, left). To probe the size of the particles in solution under conditions relevant to our ligand exchange reactions, we collected dynamic light scattering (DLS) measurements on GCC-Ru in DMSO, the solvent used for the ligand exchange reactions. The DLS data reveal GCC-Ru consists of particles with an average hydrodynamic radius of 64 nm with 8 % polydispersity (Figure S1, right). Together, the TEM and DLS data indicate that GCC-Ru consists of a relatively uniform population of carbon nanoparticles.

Scheme 1. Synthesis of complexes and surface functionalization procedure.

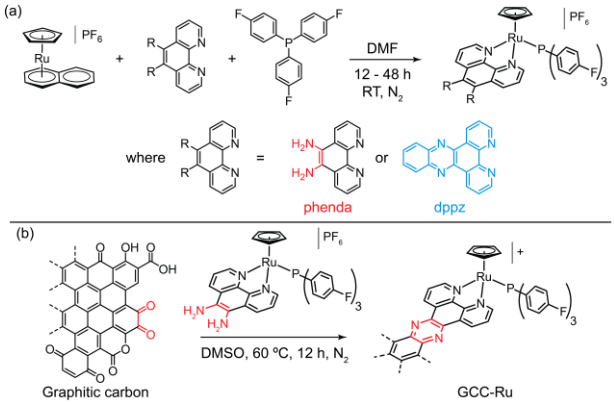

Cyclic voltammetry on functionalized glassy carbon plate electrodes evinces formation of the pyrazine linkage under functionalization conditions. This linkage undergoes a two-proton, two-electron redox process in aqueous media[37-43]. The appearance of new redox features in the cyclic voltammogram of a functionalized electrode reveals formation of the surface pyrazine (Figure S2). Indeed, we observe a feature centered at −0.024 V vs the reversible hydrogen electrode, consistent with previous literature values for this linkage.[37-43] Thus, the functionalization procedure results in the formation of the pyrazine linkage necessary to engender strong electronic coupling to the Ru center.

X-ray photoelectron spectroscopy (XPS) reveals incorporation of the molecular complex into the surface. The survey spectrum of GCC-Ru functionalized on carbon plates shows the appearance of features corresponding to N 1s, F 1s, P 2p, and Ru 3p transitions that are absent for unfunctionalized carbon (Figure S3). High-resolution scans of the N 1s region (Figure 2) reveal a feature that deconvolves into two peaks centered at 399.5 eV and 398.3 eV with an integration ratio of ~1:1. These peaks are in line with those expected for metal-bound pyridinic and pyrazinic nitrogen environments.[37,41,44] Integration of the N 1s peak manifold against the Ru $3p_{3/2}$ feature yields a N:Ru ratio of 5:1, close to the expected value of 4:1. Surprisingly, high-resolution scans reveal only one F 1s peak at 686.9 eV and a single P 2p doublet at 131.7 and 130.8 eV, consistent with expected values for a metal bound phosphine but not for PF_6^-.[45,46] The integration of these peaks yields a F:P ratio of 4:1, indicating that the expected ratio of 3:1 in PAr^{F}_3 is retained, but that the surface contains no detectable PF_6^- ions. We hypothesize that

the surface compensates for the loss of PF_6^- via deprotonation of surface hydroxyl or carboxyl groups or that the PF_6^- is exchanged for soluble anions undetectable over the background signal by XPS (*i.e.* OH^-, EtO^-). These elemental ratios revealed by XPS are consistent with incorporation of the $[CpRu(dppz)PAr^F_3]^+$ fragment into the surface.

Since the functionalization conditions are similar to those used for ligand exchange studies, we assessed the degree of retention of the PAr^F_3 on the Ru sites. While we observe substantial PAr^F_3 exchange on the GCC-Ru plates (see SI for details) we observe good retention of PAr^F_3 on the GCC-Ru powders used for kinetic studies below. Bulk elemental analyses of the high surface area GCC-Ru powder samples reveal an N:F ratio of 1.4 ± 0.4 and a Ru:P ratio of 1 ± 0.2, in good agreement with the expected ratios for incorporation of the $[CpRu(dppz)PAr^F_3]^+$ fragment onto the surface and consistent with retention of PAr^F_3 at a majority of Ru sites (see Table S1 for analysis of all samples). However, due to the error in the elemental analysis data we cannot exclude a minor population of exchanged sites on the high surface area GCC-Ru samples. Together, the XPS and bulk elemental analysis data indicate that GCC-Ru predominantly contains PAr^F_3-bound Ru sites.

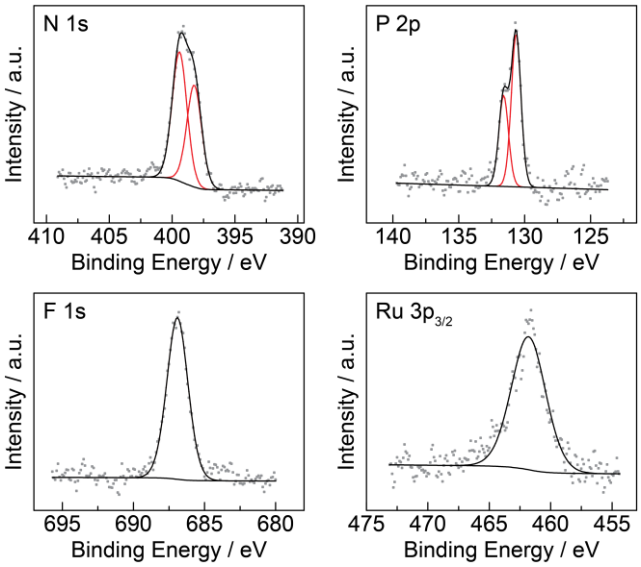

Figure 2. High resolution XPS spectra of GCC-Ru. Gray dots are the measured data while black lines are the fit background and peak manifolds. Where more than one peak is fit to the manifold, the constituent peaks are shown in red.

As ligand substitution rates are dependent on oxidation state of the metal center,[47-49] we used X-ray absorption near edge structure (XANES) and electron paramagnetic resonance (EPR) spectroscopies to determine the Ru oxidation state in GCC-Ru. The position of the rising edge in the XANES region provides a direct measure of oxidation state.[50] The Ru K-edge spectrum of the molecular reference $[CpRu(dppz)PAr^F_3]^+$ shows a rising edge with an inflection point at 22123.3 eV whereas the GCC-Ru spectrum shows a 0.3 eV blue shift to 22123.6 eV (Figure S4) which is also preserved following ligand exchange (Figure S4). In general, Ru(II) to Ru(III) oxidation leads to a 1–2 eV blue shift in the edge inflection point,[37,51] which is much larger than the shift observed for GCC-Ru. This attenuated blue shift could indicate the presence of a minor population of formally oxidized Ru(III) sites giving rise to a slightly shifted average signal. To investigate this possibility, we collected EPR spectra to probe the ensemble of Ru oxidation states since oxidation to Ru^{3+} generates a d^5 electronic configuration which would be expected to be EPR active. The EPR spectrum of GCC-Ru shows only one feature with a *g* value of 2.005, consistent with the measured value of 2.005 for the unpaired spin density found in graphitic carbons (Figure S5). Thus, we conclude that the majority population of GCC-Ru remains Ru^{2+} upon conjugation. Thus, we attribute the 0.3 eV shift in the XANES inflection as indicative of increase in partial positive charge on each Ru center in GCC-Ru induced by, perhaps, the lower LUMO level of the conjugated phen ligand.

Extended X-ray absorption fine structure (EXAFS) reveals the retention of the coordination environment of GCC-Ru upon conjugation. EXAFS results from the scattering of photoelectrons off nearby atoms to provide a fingerprint for the coordination environment about the metal center. Comparison of the EXAFS spectrum for high surface area carbon powder GCC-Ru (Figure 3, red) with that of $[CpRu(dppz)PAr^F_3]^+$ (Figure 3, blue) reveals a slight decrease in intensity of the *R*-space peak at 1.66 Å. This small change in the spectrum is consistent with the slight loss of PAr^F_3 indicated by the elemental analysis. Minority exchange of PAr^F_3 (see above) for a light atom donor of a solvent molecule would give rise to a less intense first scattering peak. Nonetheless, the EXAFS data in tandem with the XPS and bulk elemental analysis results are consistent with predominant retention of the coordination environment upon functionalization.

To ensure that the ligand exchange procedure does not result in decomposition of the GCC-Ru sites, post-mortem analysis was also performed on the carbon powders following ligand exchange for 130 hours at 110 °C (See SI for details). The exchanged GCC-Ru EXAFS spectrum (Figure 3, dashed black) is nearly identical with that of $[CpRu(dppz)PAr^F_3]^+$ (Figure 3, blue). Thus, we conclude that the ligand exchange process on the surface results in clean conversion of all GCC-Ru sites to a phosphine-bound species and no substantial decomposition of GCC-Ru occurs under the examined conditions.

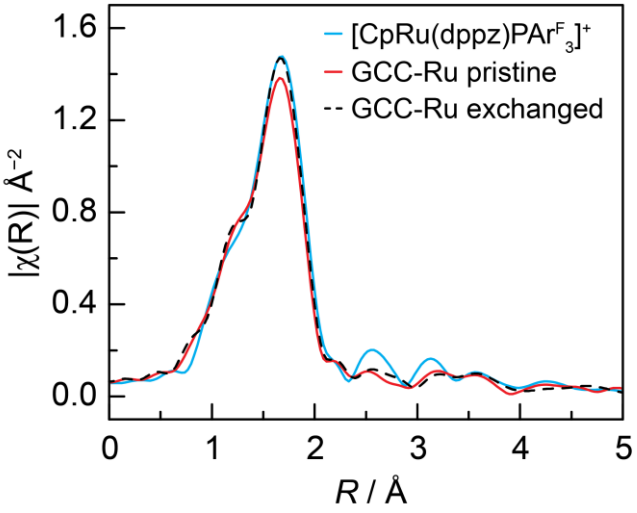

Figure 3. EXAFS spectra of $[CpRu(dppz)PAr^F_3]^+$ (blue), GCC-Ru (red) and post-exchange GCC-Ru after 130 hours of phosphine exchange at 110 °C (black, dashed).

Kinetic Measurement of Phosphine Exchange

Scheme 2. Ligand exchange reactions.

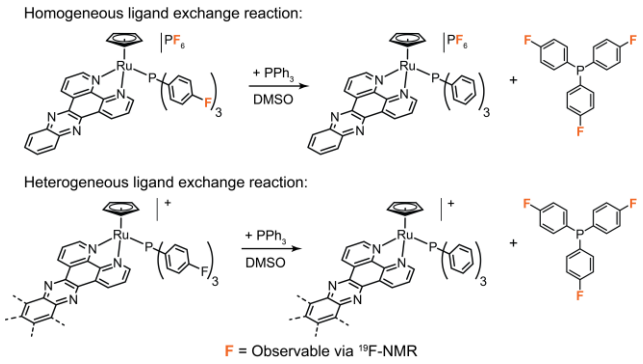

Scheme 2. Ligand exchange reactions on the molecular (top) and heterogeneous GCC-Ru (bottom) complexes. For both, the F atoms observable by ^{19}F-NMR and tracked for kinetic measurements are highlighted in orange.

The rate of exchange of PAr^{F}_3 for PPh_3 on the molecular complexes was monitored via ^{19}F-NMR (Scheme 2). ^{1}H-NMR is not amenable to this analysis because the proton resonances on the complex do not shift enough upon phosphine exchange to integrate cleanly. Furthermore, addition of large excesses of the incoming PPh_3 ligand overwhelms any other signals in the aromatic region. Though four distinct resonances for free and complexed PAr^{F}_3 and PPh_3 are observed in ^{31}P-NMR, this technique is not amenable to monitoring the ligand exchange due to the relatively low NMR sensitivity for the ^{31}P nucleus. Indeed, we can observe peaks corresponding to free PAr^{F}_3 in the ^{19}F-NMR spectra at the earliest time points of the ligand exchange reaction but the corresponding peaks in the ^{31}P-NMR spectra are not significantly above background until after the ligand exchange reaction has progressed for many hours. Over the course of the reaction, we observe a decrease in intensity of the ^{19}F signal for $[CpRu(dppz)PAr^{F}_3]^+$ at –109.9 ppm and the growth of a peak at –111.8 ppm that corresponds to the free PAr^{F}_3 (Figure 4, top). Integration of these features allows the construction of half-lives vs time plots which indicate first order behavior (Figure 4, bottom). We extract k and $t_{1/2}$ from the slopes of linear fits to these plots.

The rate of exchange on the heterogeneous GCC-Ru complexes was also monitored via ^{19}F-NMR (Scheme 2). ^{1}H- and ^{31}P-NMR are not informative due to the presence of excess PPh_3 and the low sensitivity to the ^{31}P nucleus (Figure S6). In brief, we collected aliquots from a stirred suspension of the GCC-Ru powder in DMSO containing excess PPh_3. The amount of liberated PAr^{F}_3 was quantified against an internal standard of KPF_6 via ^{19}F-NMR (see SI for details). Although a minority of sites on the surface may undergo exchange during functionalization, this procedure of monitoring the liberated PAr^{F}_3 allows us to exclude convolution from that possible subpopulation. Over the course of the reaction, we observe the growth of a peak at –111.8 ppm that corresponds to the free PAr^{F}_3 as well as a peak at –106.9 ppm that corresponds to $OPAr^{F}_3$ which results from carbon-mediated O-atom transfer from DMSO during the reaction as discussed below (Figure 5, top). To construct half-lives vs time plots (Figure 5, bottom), we summed the integration of both features to account for all liberated PAr^{F}_3. As for the molecular complex, these plots indicate first order kinetics and linear fits to these data yield k and $t_{1/2}$.

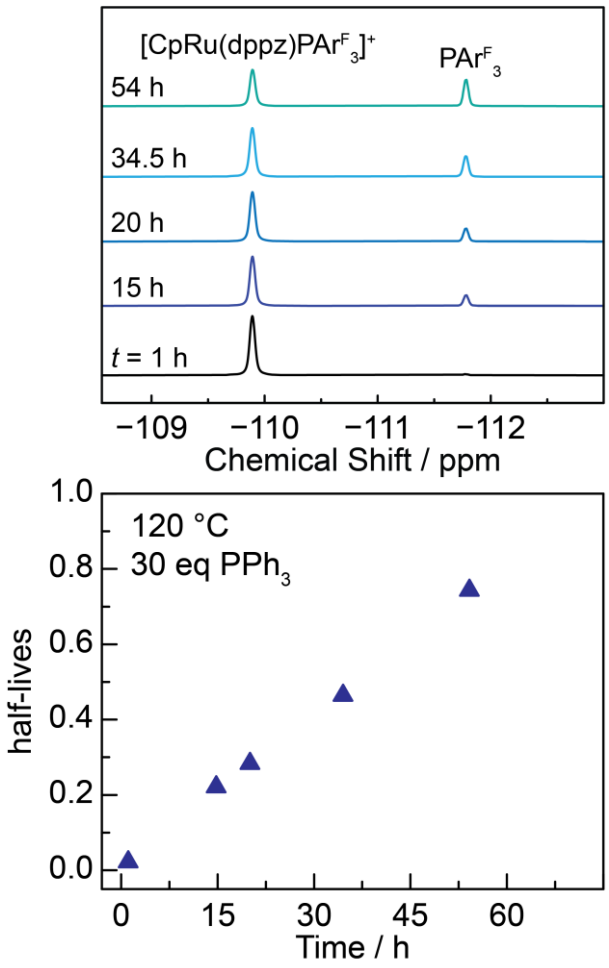

Figure 4. Representative ^{19}F-NMR spectral region of interest for the ligand exchange reaction at 120 °C for the molecular complex (top) and the corresponding half-lives versus time plot showing the reaction progress (bottom). The corresponding full spectra are given in the SI.

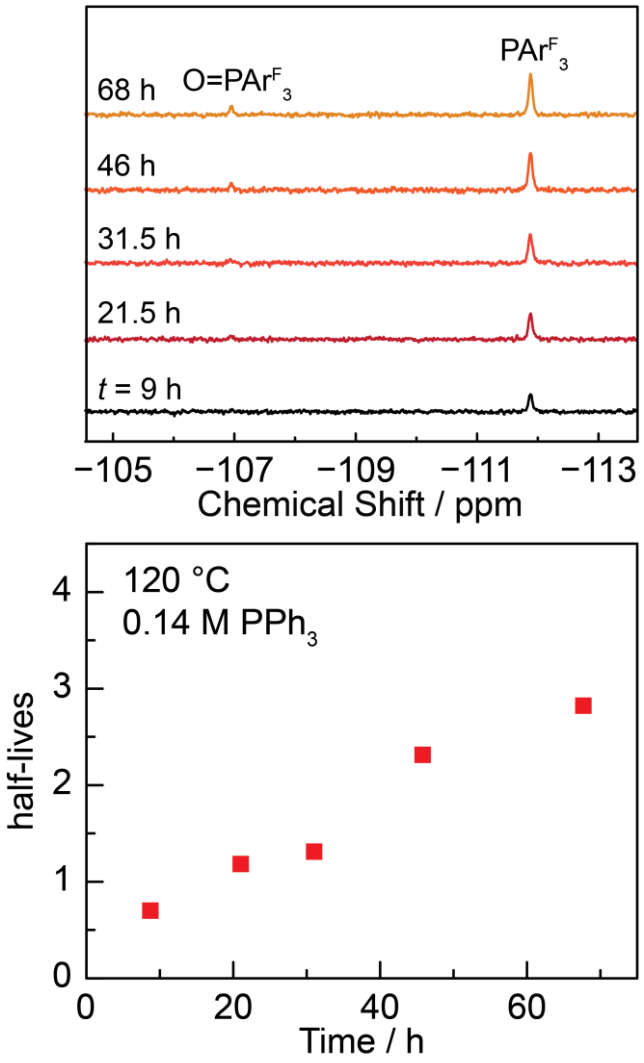

Figure 5. Representative ^{19}F-NMR spectral region of interest for the ligand exchange reaction at 120 °C for GCC-Ru (top) and the corresponding half-lives versus time plot showing the reaction progress (bottom). The corresponding full spectra are given in the SI.

Scheme 3. Dissociative mechanisms

(a)

$$[CpRu(dppz)PAr^F_3]^+ \xrightarrow[RLS]{k} [CpRu(dppz)]^+ + PAr^F_3$$

(b)

$$[CpRu(dppz)PAr^F_3]^+ + PPh_3 \underset{}{\overset{K_a}{\rightleftharpoons}} [CpRu(dppz)\text{ - - }PAr^F_3]^+ \text{ - - - } PPh_3$$

$$[CpRu(dppz)\text{ - - }PAr^F_3]^+ \text{ - - - } PPh_3 \xrightarrow[RLS]{k_f} [CpRu(dppz)PPh_3]^+ + PAr^F_3$$

Ligand exchange on [CpRu(dppz)PAr$^F_3$]$^+$ proceeds through a dissociative mechanism (Scheme 3a). [CpRu(dppz)PAr$^F_3$]$^+$ exhibits zero-order dependence on the concentration of the incoming PPh$_3$ ligand (Figure 6, top) over a large range of [PPh$_3$], from 0.009 to 0.48 M. Even at low [PPh$_3$] (0.5 equivalents, ca. 10^{-2} M), the rate constant shows no dependence on [PPh$_3$], consistent with a dissociative ligand exchange mechanism.[47,49] An alternative mechanistic possibility that must be considered is a dissociative interchange mechanism in which outer-sphere pre-association between [CpRu(dppz)PAr$^F_3$]$^+$ and PPh$_3$ is followed by rate limiting interchange substitution (Scheme 3b).[47,48] This interchange mechanism gives rise to the following expression for k_{obs}:[52]

$$k_{obs} = \frac{k_f K_a[PPh_3]}{1 + K_a[PPh_3]} \quad (1)$$

which limits to a zero order dependence on [PPh$_3$] when K_a[PPh$_3$] is much greater than 1. The observed zero order dependence in [PPh$_3$] even at 10^{-2} M PPh$_3$ necessitates an outer-sphere association constant, K_a, on the order of 10^4 M^{-1}. While electrostatic interactions lead to pre-association constants of 10^1-10^4 for ion pairs in DMSO,[53] these values are out of the range for the cation-neutral pre-association that would be required for interchanges substitution in this system. Thus, the observed zero order dependence of [PPh$_3$] is most consistent with a simple dissociate substitution mechanism with following rate law:[47,48]

$$rate = k[CpRu(dppz)PAr^F_3PF_6] \quad (2)$$

Additionally, relaxed coordinate scans at the ωB97X-D3/def2-TZVPP[54] level of theory from 2.4 to 7.4 Å for the dissociation of the phosphine ligand from [CpRu(dppz)PAr$^F_3$]$^+$ indicate an extremely late transition state for the cleavage of the Ru–P bond (Figure S7), consistent with a dissociative mechanism. Together, the experimental and computational data support a dissociative mechanism involving rate-limiting Ru–P bond cleavage.

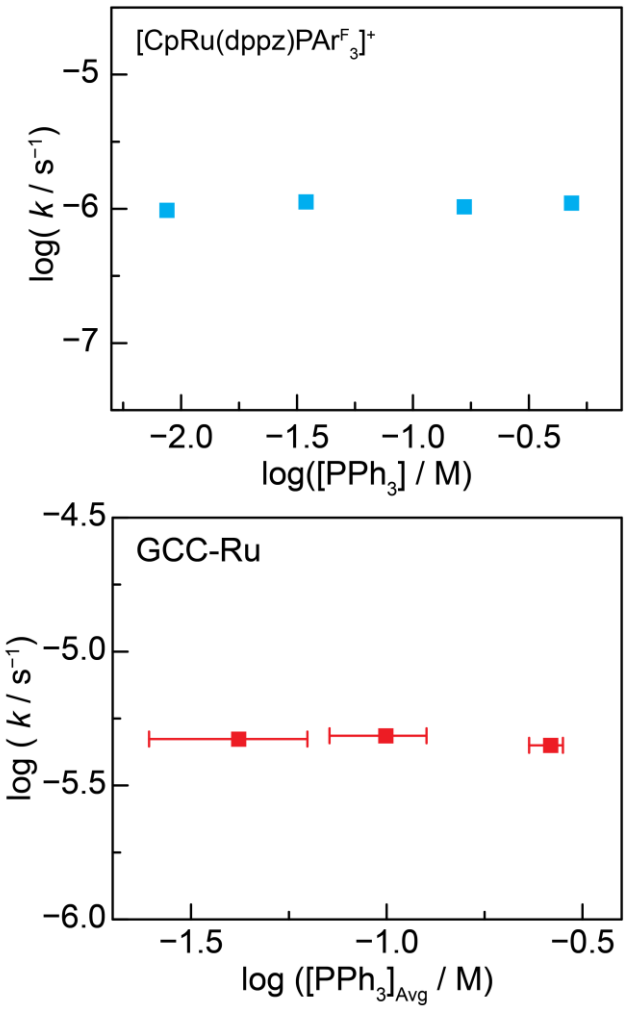

Figure 6. Reaction order plots for the dependence of the ligand exchange rate constants on [PPh_3] for the molecular complex (top) and GCC-Ru (bottom). The error bars on the bottom plot correspond to the total variation in [PPh_3] during the ligand exchange reaction on GCC-Ru.

Order data also points to dissociative ligand substitution for GCC-Ru. The rate of exchange for GCC-Ru also exhibits zero-order dependence on the initial [PPh_3] over the range 0.071 to 0.297 M. We note that the substitution reaction occurs concurrently with background conversion of PPh_3 to $OPPh_3$. This background reactivity also results in conversion of free $PAr^F{}_3$ to $OPAr^F{}_3$, as observed in the ^{19}F-NMR spectra of the GCC-Ru ligand exchange reaction (Figure 5). This side reaction occurs at a similar rate as ligand exchange and approaches pseudo-equilibrium during the time course of ligand exchange (Figure S8). Importantly, conversion of PPh_3 to $OPPh_3$ was observed even after exhaustive removal of trace O_2 (See SI for details) and is instead attributed to carbon-mediated background O-atom transfer from DMSO to PPh_3. Control experiments reveal that unfunctionalized carbon catalyzes O-atom transfer from DMSO to PPh_3 with concurrent formation of dimethyl sulfide observed by GC-MS and NMR (Figure S9 and S10). To account for this background reaction, we determined the order by using the average [PPh_3] measured during the course of ligand exchange reaction and denote the overall variation in [PPh_3] during the reaction with error bars in the bottom panel of Figure 6. Despite this variation, over the range 0.043 to 0.263 M, we still observe zero-order dependence on PPh_3. Given the lower limit of this range, a dissociative interchange mechanism for GCC-Ru requires K_a on the order of 10^3 M^{-1}, which is well above the range expected for interaction of a cation with a neutral species.[53] Therefore, the observed order in [PPh_3] for GCC-Ru is most consistent with a simple dissociative mechanism. Together the above kinetic analysis suggests that both GCC-Ru and the Ru molecule undergo a dissociative substitution mechanism with rate-limiting cleavage of the Ru–P bond.

Model for rate and activation metric differences

The above spectroscopic and kinetic data indicate that GCC-Ru and the molecular analog consist of identical local structures with common substitution mechanisms. Thus, this comparison provides an ideal platform for isolating the impact of the interfacial local environment beyond the binding site on the kinetics of ligand exchange.

We find that GCC-Ru exhibits a two- to three-fold greater ligand exchange rate than the Ru molecule. The rate constants and half-lives for each complex as a function of temperature are reported in Table 1 and Table 2, respectively. The change in ligand electronics that derives from access to the much larger pi-manifold upon conjugation may influence the observed rate difference. To probe the impact of changing the size of the pi-manifold of the bis(imine) ligand, we also examined the rate of exchange on [CpRu(phen)$PAr^F{}_3$]$^+$ (see SI for synthetic details). Both [CpRu(phen)$PAr^F{}_3$]$^+$ and [CpRu(dppz)$PAr^F{}_3$]$^+$ exhibit similar ligand exchange rates, within a factor of 0.8 and 1.3 depending on temperature (Tables S2 and S3, Figure S11). The minimal difference in exchange rates between these two molecular species suggest that the size of the pi-manifold of the bis(imine) ligand cannot solely account for the majority of the rate enhancement for GCC-Ru.

Table 1. Summary of rate constants for ligand exchange reactions

Compound	k s^{-1} x 10^{-8} (80 °C)	k s^{-1} x 10^{-8} (90 °C)	k $^{-1}$ x 10^{-8} (100 °C)	k $^{-1}$ x 10^{-8} (110 °C)	k $^{-1}$ x 10^{-8} (120 °C)
GCC-Ru	N/A[a]	22 ± 1	80 ± 10	290 ± 20	900 ± 300
[CpRu(dppz)$PAr^F{}_3$]$^+$	2.45 ± 0.05	8.92 ± 0.09	30.6 ± 0.7	106 ± 2	250 ± 10

[a] Useful data not obtained, conversion yielded too low [$PAr^F{}_3$]$_{free}$ to integrate reliably.

Table 2. Summary of half-lives for ligand exchange reactions

Compound	$t_{1/2}$ h (80 °C)	$t_{1/2}$ h (90 °C)	$t_{1/2}$ h (100 °C)	$t_{1/2}$ h (110 °C)	$t_{1/2}$ h (120 °C)
GCC-Ru	N/A[a]	897 ± 43	259 ± 47	66 ± 4	25 ± 7
[CpRu(dppz)$PAr^F{}_3$]$^+$	7865 ± 144	2158 ± 23	631 ± 14	182 ± 5	78 ± 3

[a] Useful data not obtained, conversion yielded too low [$PAr^F{}_3$]$_{free}$ to integrate reliably.

Table 3. Activation metrics of ligand exchange.

Compound	**$\Delta H^‡$** kcal mol^{-1}	**$\Delta S^‡$** cal $mol^{-1}K^{-1}$	**$\Delta G^‡$ at 120 °C** kcal mol^{-1}
[CpRu(dppz)$PAr^F{}_3$]$^+$	32.3 ± 0.7	−2 ± 2	33.2 ± 1
GCC-Ru	35.1 ± 0.5	7 ± 1	32.3 ± 0.6

Temperature dependent measurements of k reveal differences in the reaction activation parameters between the molecule and GCC-Ru. The enthalpies of activation, $\Delta H^‡$, were extracted from the slopes of Eyring plots of data collected from 80 to 120 °C (Figure 7, Figures S12-S22). [CpRu(dppz)$PAr^F{}_3$]$^+$ displays a $\Delta H^‡$ of 32.3 ± 0.7 kcal mol^{-1} whereas GCC-Ru displays a ~3 kcal/mol larger value of 35.1 ± 0.5 kcal mol^{-1} (Table 3). As expected for dissociative substitution reaction in general, both complexes show large positive $\Delta H^‡$ values that correspond predominantly to the enthalpy of Ru–P bond cleavage.[55-57] Thus, the increased $\Delta H^‡$ for the GCC-Ru relative to the molecular analog implies surface conjugation slightly increases the Ru–P bond strength. This stronger bond is attributed to a slightly more electropositive Ru center in GCC-Ru, as indicated by the blue-shift in the Ru K-edge spectrum of GCC-Ru relative to [CpRu(dppz)$PAr^F{}_3$]$^+$, see above. Despite the stronger Ru–P bond, GCC-Ru still displays a faster ligand exchange rate.

Given the enthalpically stronger Ru–P bond in GCC-Ru, the rate enhancement must result from entropic contributions. The entropy of activation for each complex was determined from the intercepts of the Eyring plots of the rate data for GCC-Ru and

[CpRu(dppz)PAr$^{F}_{3}$]$^{+}$ (Figure 7, Figures S12-S22). $\Delta S^{\ddagger}$ for [CpRu(dppz)PAr$^{F}_{3}$]$^{+}$ is -2 ± 2 cal mol^{-1}K^{-1} (Table 3). Since the determination of accurate entropy values from the extrapolation of linear fit lines is challenging, we measured each data point at least in triplicate and the error bars on the reported entropy values derive from a linear regression that propagates the error from each data point. Though unusual, small negative values of $\Delta S^{\ddagger}$ for dissociative exchange reactions have precedent.[58-61] We attribute this small negative value for the Ru molecule to perturbations to the solvation shell that occur as the Ru–P bond lengthens into the transition state. Importantly, this Ru complex bears an overall positive charge which orients DMSO dipoles.[62] As the Ru–P bond lengthens, the volume of the complex increases,[63] which necessitates more DMSO molecules to enter the solvation shell (Figure 8, top). This increased solvent ordering is sufficient to counteract the favorable entropy change associated with Ru–P bond extension,[47,49] leading to a slightly negative entropy in aggregate. Indeed, for neutral Ru half-sandwich complexes in non-polar media, where these solvent ordering effects are expected to be minimal, the reactions display the expected large positive $\Delta S^{\ddagger}$ values.[55]

In contrast to the slightly negative activation entropy for the Ru molecule, GCC-Ru exhibits a positive $\Delta S^{\ddagger}$ of 7 ± 1 cal mol^{-1}K^{-1} (Table 3). This value is slightly lower than typical for dissociative ligand exchange reactions[54] but is significantly higher and of opposite sign to that for [CpRu(dppz)PAr$^{F}_{3}$]$^{+}$. Given that the slightly negative activation entropy for the molecule is attributed to solvent ordering in the transition state, we attribute the higher $\Delta S^{\ddagger}$ for GCC-Ru to differential solvation environments for the surface bound site relative to the discrete molecule. In particular, the mobile free carriers in the carbon[64] render it highly polarizable and, therefore, able to screen the local positive charge of the molecular site. Since the Ru fragment and the carbon are inherently co-solvated,[37] the polarizability of the carbon serves to distribute the charge of the appended molecular site over the carbon host (Figure 8, bottom) and respond to changes in the local charge at that site along the reaction coordinate. We posit that this effect increases the activation entropy by reducing the requirement for DMSO solvent ordering as the activation volume increases during Ru–P bond extension in the transition state (Figure 8, bottom). This increase in activation entropy fosters faster ligand exchange. Indeed, the charge density of *s*-block metals correlates inversely with their water exchange rates[47] and the surface charge density of polarized electrodes inversely correlates with the rate of solvent exchange.[65] Together, the above discussion emphasizes the role of the conductive carbon in altering the activation entropy for surface ligand exchange reactions.

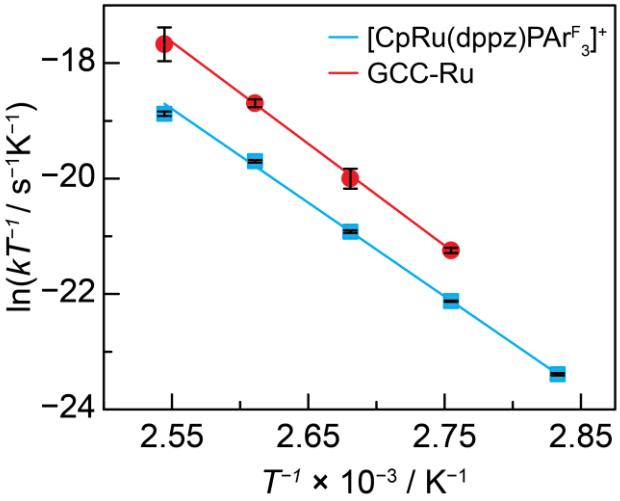

Figure 7. Eyring plot for exchange of PAr$^{F}_{3}$ for PPh$_3$ on GCC-Ru (red) and [CpRu(dppz)PAr$^{F}_{3}$]$^{+}$ (blue). Error bars (black) represent the standard error from measurements of at least 3 trials per point. The best fit line derives from a linear regression that incorporates the error at each point.

The above discussion highlights that, although conjugation serves to increase the Ru–P bond strength and the corresponding $\Delta H^{\ddagger}$, the enhanced solvating properties of the carbon provide for an increased $\Delta S^{\ddagger}$ that more than offsets the change in Ru–P bond strength. These two compensating effects lead to a very slight decrease in $\Delta G^{\ddagger}$ from 33.2 ± 1 kcal mol^{-1} for the Ru molecule to and 32.3 ± 0.6 kcal mol^{-1} for GCC-Ru at 120 °C (Table 3). This small difference is consistent with the observed two- to three-fold rate enhancement observed for GCC-Ru and results from countervailing changes to entropies and enthalpies of activation.

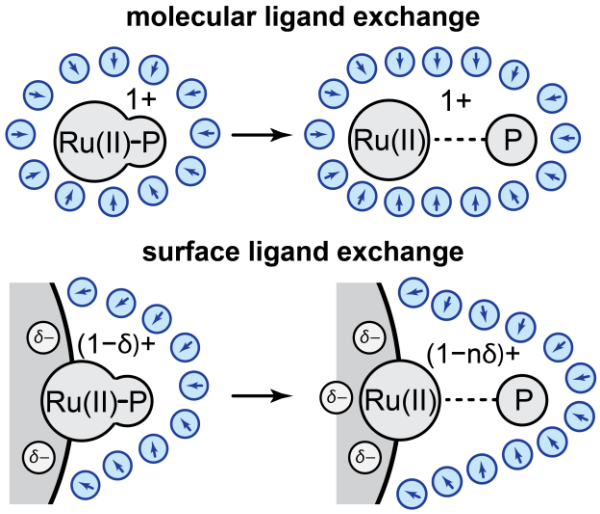

Figure 8. Cartoon comparing ligand exchange for the molecular and surface exchange reactions.

Conclusion

We report a model system that enables the direct comparison of the activation parameters for a dissociative ligand exchange reaction proceeding at molecular and surface sites of identical local structure. This system has allowed us, for the first time, to isolate the role of the surface on the enthalpic and entropic contributions to the reaction barrier for ligand exchange. The surface species, GCC-Ru, has a higher $\Delta H^{\ddagger}$, consistent with a more

electropositive Ru center. Despite the stronger Ru–P bond, we observe faster ligand exchange rates for the surface species than for the molecular analog. The rate enhancement derives from a more positive $\Delta S^{\ddagger}$ for the surface species that we attribute to more effective charge screening by the surface. Since the band structure of the carbon and the molecule structure of the appended site can be tuned independently, the GCC platform provides an ideal model system to probe the factors which govern the entropic and enthalpic contributions of exchange kinetics, thereby providing a path towards the rational understanding of ligand exchange processes on nanomaterials.

ASSOCIATED CONTENT

Supporting Information

The Supporting Information is available free of charge on the ACS Publications website.

Full experimental details, synthetic procedures as well as XPS, XAS, EPR, electrochemical, computational and kinetic data.

Corresponding Author

*yogi@mit.edu

Present Addresses

R.I.S. – Departamento de Química, Centro de Investigación y Estudios Avanzados (Cinvestav), Av. Instituto Politécnico Nacional 2508, 07360 D.F., México.
S.O. – Chemistry Division, Brookhaven National Laboratory, Upton, New York 11973, United States.

Author Contributions

ø These authors contributed equally.

Notes

The authors declare no competing financial interests.

ACKNOWLEDGMENT

The authors thank Jeffrey Rosenberg and Mohan Kumar for assistance with the GC-MS measurement; Bruce Adams, Walt Massefski and John Grimes for help with the NMR experiments; Dr. Adam Graham for assistance in the collection of TEM images; and Hursh Sureka and Prof. Bradley Olsen for access to and assistance in measuring DLS. This research was supported by the U.S. Department of Energy, Office of Science, Office of Basic Energy Sciences, under award number DE-SC0014176. The EPR spectroscopy work was supported by the NIH-NIHGMS through grant number 1R35GM126961-01. C.J.K and S.O. acknowledge support from the National Science Foundation Graduate Research Fellowship program under Grant No. 1122374. PWS is supported by an Arnold O. Beckman Postdoctoral Fellowship. Use of the Advanced Photon Source is supported by the U.S. Department of Energy, Office of Science, and Office of Basic Energy Sciences, under Contract DE-AC02-06CH11357. MRCAT operations are supported by the Department of Energy and the MRCAT member institutions. This work made use of Shared Experimental Facilities supported in part by the MRSEC Program of the National Science Foundation under award no. DMR-1419807 and was performed in part at the Center for Nanoscale Systems, a member of the National Nanotechnology Coordinated Infrastructure Network, which is supported by the National Science Foundation under NSF award no. 1541959. Y.S. acknowledges the Sloan Foundation, Research Corporation for Science Advancement (Cottrell Scholar), and the Canadian Institute for Advanced Research (CIFAR Azrieli Global Scholar).

REFERENCES

1. Kilmartin, J.; Sarip, R.; Grau-Crespo, R.; Di Tommaso, D.; Hogarth, G.; Prestipino, C.; Sankar, G. Following the Creation of Active Gold Nanocatalysts from Phosphine-Stabilized Molecular Clusters. *ACS Catal.* **2012**, *2*, 957– 963.
2. Ung, D.; Murphy, I. A.; Cossairt, B. M. Designing nanoparticle interfaces for inner-sphere catalysis. *Dalton Trans.*, **2020**,*49*, 4995-5005.
3. Rossi, L. M.; Fiorio, J. L.; Garcia, M. A. S.; Feraz, C. P. The role and fate of capping ligands in colloidally prepared metal nanoparticle catalysts. *Dalton Trans.*, **2018**, *47*, 5889-5915.
4. Eswaramoorthy, S., Sakthivel, N. A.; Dass, A. Core Size Conversion of Au329(SCH2CH2Ph)84 to Au279(SPh-tBu)84 Nanomolecules. *J. Phys. Chem. C* **2019**, *123*, 9634–9639.
5. Sperling, R. A.; Parak, R. J. Surface modification, functionalization and bioconjugation of colloidal inorganic nanoparticles. *Phil. Trans. R. Soc. A* **2010**, *368*, 1333–1383.
6. Mozaffari, S.; Li, W.; Dixit, M.; Seifert, S.; Lee, B.; Kovarik, L.; Mpourmpakis, G.; Karim, A. M. The role of nanoparticle size and ligand coverage in size focusing of colloidal metal nanoparticles. *Nanoscale Adv.*, **2019**, *1*, 4052-4066.
7. Cheng, H., Yang, N., Liu, G., Ge, Y., Huang, J., Yun, Q., Du, Y., Sun, C.-J., Chen, B., Liu, J., Zhang, H., Ligand-Exchange-Induced Amorphization of Pd Nanomaterials for Highly Efficient Electrocatalytic Hydrogen Evolution Reaction. *Adv. Mater.* **2020**, *32*, 1902964.
8. Wu, Z.; Yang, S.; Wu, W. Shape control of inorganic nanoparticles from solution. *Nanoscale*, **2016**, *8*, 1237-1259.
9. Xia, Y., Xiong, Y., Lim, B. and Skrabalak, S. Shape-Controlled Synthesis of Metal Nanocrystals: Simple Chemistry Meets Complex Physics?. *Angew. Chem. Int. Ed.,* **2009**, *48,* 60-103.
10. Wang, G.; Huang, T.; Murray, R. W.; Menard, L.; Nuzzo, R. Near-IR Luminescence of Monolayer-Protected Metal Clusters. *J. Am. Chem. Soc.* **2005**, *127*, 812–813.
11. Wu, Z.; Jin, R. On the Ligand's Role in the Fluorescence of Gold Nanoclusters. *Nano Lett.* **2010**, *10*, 2568–2573.
12. Shibu, E.S.; Muhammed, H.; Tsukuda, T.; Pradeep, T. Ligand Exchange of Au25SG18 Leading to Functionalized Gold Clusters: Spectroscopy, Kinetics, and Luminescence. *J. Phys. Chem. C* **2008**, *112*, 12168–12176.
13. Anderson, N. C.; Owen, J.S. Soluble, Chloride-Terminated CdSe Nanocrystals: Ligand Exchange Monitored by 1H and 31P NMR Spectroscopy. *Chem. Mater.* **2013**, *25*, 69–76.
14. Ji, X.; Copenhaver, D.; Sichmeller, C.; Peng, X. Ligand Bonding and Dynamics on Colloidal Nanocrystals at Room Temperature: The Case of Alkylamines on CdSe Nanocrystals. *J. Am. Chem. Soc.* **2008**, *130*, 5726–5735.
15. De Roo, J.; Ibanez, M.; Geiregat, P.; Nedelcu, G.; Walravanes, W.; Maes, J.; Martins, J. C.; Van Driessche, I.; Kovalenko, M. V.; Hens, Z. *ACS Nano* **2016**, *10*, 2071–2081.
16. Heuer-Jungermann, A.; Feliu, N.; Bakaimi, I.; Hamaly, M.; Alkilany, A.; Chakraborty, I.; Masood, A.; Casula, M. F.; Kostopoulou, A.; Oh, E.; Susumu, K.; Stewart, M. H.; Medintz, I. L.; Stratakis, E.; Parak, W. J.; Kanaras, A. G. The Role of Ligands in the Chemical Synthesis and Applications of Inorganic Nanoparticles. *Chem. Rev.* **2019**, *119*, 4819–4880.
17. Kanelidis, I.; Kraus, T. The role of ligands in coinage-metal nanoparticles for electronics. *Beilstein J Nanotechnol.* **2017**, *8*, 2625–2639.
18. Sardar, R.; Funston, A. M.; Mulvaney, P.; Murray, R. W. Gold Nanoparticles: Past, Present, and Future. *Langmuir*, **2009**, *25*, 13840–13851.
19. Holland, G. P.; Sharma, R.; Agola, J. O.; Amin, S.; Solomon, V. C.; Singh, P.; Buttry, D. A.; Yarger, J. L. NMR Characterization of Phosphonic Acid Capped SnO_2 Nanoparticles *Chem. Mater.* **2007**, *19*, 2519–2526.

20. Ritchhart, A.; Cossairt, B. M. Quantifying Ligand Exchange on InP Using an Atomically Precise Cluster Platform. *Inorg. Chem.* **2019**, *58*, 2840–2847.
21. Hostetler, M. J.; Templeton, A. C.; Murray, R. W. Dynamics of Place-Exchange Reactions on Monolayer-Protected Gold Cluster Molecules. *Langmuir* **1999**, *15*, 3782–3789.
22. Uznanski, P.; Kurjata, J.; Bryszewska, E. Modification of gold nanoparticle surfaces with pyrenedisulfide in ligand-protected exchange reactions. *Materials Science-Poland,* **2009**, *27*, 659-670.
23. Hakkinen, H. The gold–sulfur interface at the nanoscale. *Nature Chem.* **2012,** *4*, 443–455.
24. Anderson, N. C.; Hendricks, M. P.; Choi, J. J.; Owen, J. S. Ligand Exchange and the Stoichiometry of Metal Chalcogenide Nanocrystals: Spectroscopic Observation of Facile Metal-Carboxylate Displacement and Binding. *J. Am. Chem. Soc.* **2013**, *135*, 18536–18548.
25. Donkers, R. L.; Song, Y.; Murray, R. W. Substituent Effects on the Exchange Dynamics of Ligands on 1.6 nm Diameter Gold Nanoparticles. *Langmuir* 2004, 20, 11, 4703–4707.
26. Ionita, P.; Caragheorgheopol, A.; Gilbert, B. C.; Chechik, V. Mechanistic Study of a Place-Exchange Reaction of Au Nanoparticles with Spin-Labeled Disulfides. *Langmuir* **2004**, *20*, 11536–11544.
27. Guo, R.; Song, Y.; Wang, G.; Murray, R. W. Does Core Size Matter in the Kinetics of Ligand Exchanges of Monolayer-Protected Au Clusters?. *J. Am. Chem. Soc.* **2005**, *127*, 2752–2757.
28. Kessler, M. L.; Dempsey, J. L. Mapping the Topology of PbS Nanocrystals through Displacement Isotherms of Surface-Bound Metal Oleate Complexes. *Chem. Mater.* **2020**, *32*, 2561–2571.
29. Kroupa, D.M.; Anderson, N. C.; Castaneda, C. V.; Noziik, A. J.; Beard, M. C. In situ spectroscopic characterization of a solution-phase X-type ligand exchange at colloidal lead sulphide quantum dot surfaces. *Chem. Commun.*, **2016**, *52*, 13893-13896.
30. Anderson, N. C.; Chen, P. C.; Buckley, A. K.; De Roo, J.; Owen, J. S. Stereoelectronic Effects on the Binding of Neutral Lewis Bases to CdSe Nanocrystals. *J. Am. Chem. Soc.* **2018**, *140*, 7199–7205.
31. Henckel, D. A.; Enright, M. J.; Eslami, N. P. Kroupa, D. N.; Gamelin, D. R.; Cossairt, B. M. Modeling Equilibrium Binding at Quantum Dot Surfaces Using Cyclic Voltammetry. *Nano Lett.* **2020**, *20*, 2620–2624.
32. Perumal, S.; Hofmann, A.; Scholz, N.; Ruhl, E.; Graf, C. Kinetics Study of the Binding of Multivalent Ligands on Size-Selected Gold Nanoparticles. *Langmuir* **2011**, *27*, 4456–4464.
33. De Roo, J.; Yazdani, N.; Drjivers, E.; Lauria, A.; Maes, J.; Owen, J. S.; Van Driessche, I.; Niederberger, M.; Wood, V.; Martins, J.C.; Infante, I.; Hens, Z. Probing Solvent–Ligand Interactions in Colloidal Nanocrystals by the NMR Line Broadening. *Chem. Mater.* **2018**, *30,* 5485–5492.
34. Knauf, R. R.; Lennox, J. C.; Dempsey, J. L. Quantifying Ligand Exchange Reactions at CdSe Nanocrystal Surfaces. *Chem. Mater.* **2016**, *28*, 4762–4770.
35. Kessler, M. L.; Starr, H. E.; Knauf, R. R.; Rountree, K. J.; Dempsey, J. L. Exchange equilibria of carboxylate-terminated ligands at PbS nanocrystal surfaces. *Phys. Chem. Chem. Phys.*, **2018**, *20*, 23649-23655.
36. Caragheorgheopol, A.; Chechik, V. Mechanistic aspects of ligand exchange in Au nanoparticles. *Phys. Chem. Chem. Phys.*, **2008**, *10*, 5029-5041.
37. Jackson, M. N.; Oh, S.; Kaminsky, C. J.; Chu, S. B.; Zhang, G.; Miller, J. T.; Surendranath, Y. Strong Electronic Coupling of Molecular Sites to Graphitic Electrodes via Pyrazine Conjugation. *J. Am. Chem. Soc.* **2018**, *140*, 1004-1010.
38. Jackson, M. N.; Surendranath, Y. Molecular Control of Heterogeneous Electrocatalysis through Graphite Conjugation. *Acc. Chem. Res.* **2019**, *52*, 3432–3441.
39. Jackson, M. N.; Kaminsky, C.; Oh, S.; Melville, J. F.; Surendranath, Y. Graphite Conjugation Eliminates Redox Intermediates in Molecular Electrocatalysis. *J. Am. Chem. Soc.* **2019**, *141*, 14160–14167.
40. Jackson, M. N.; Pegis, M. L.; Surendranath, Y. Graphite-Conjugated Acids Reveal a Molecular Framework for Proton-Coupled Electron Transfer at Electrode Surfaces. *ACS Cent. Sci.* **2019**, *5*, 831–841.
41. Fukushima, T.; Drisdell, W.; Yano, J.; Surendranath, Y. Graphite-Conjugated Pyrazines as Molecularly Tunable Heterogeneous Electrocatalysts. *J. Am. Chem. Soc.* **2015**, *137*, 10926–10929.
42. Oh, S.; Gallagher, J. R.; Miller, J. T.; Surendranath, Y. Graphite-Conjugated Rhenium Catalysts for Carbon Dioxide Reduction. *J. Am. Chem. Soc.* **2016**, *138*, 1820–1823.
43. Kaminsky, C. J.; Wright, J.; Surendranath, Y. Graphite-Conjugation Enhances Porphyrin Electrocatalysis. *ACS Catal.* **2019**, *9*, 3667–3671.
44. Brisdon, B. J.; Griffin, G. F.; Pierce, J.; Walton, R. A. X-ray photoelectron spectra of inorganic molecules: XXX. Organometallic derivatives of tungsten(O) and tungsten(II). *J. Organomet. Chem.* **1981**, *219* (1), 53-59.
45. Shul'ga, Y. M.; Bulatov, A. V.; Gould, R. A. T.; Konze, W. V.; Pignolet, L. H. X-ray photoelectron spectroscopy of a series of heterometallic gold-platinum phosphine cluster compounds. *Inorg. Chem.* **1992,** *31*, 4704–4706.
46. Hoste, S.; Van De Vondel, D. F.; Van Der Kelen, G. P. XPS Spectra of organometallic phenyl compounds of P, As, Sb and Bi. *J. Electron Spectrosc.* **1979,** *17*, 191-195
47. Richens, D. T. Ligand Substitution Reactions at Inorganic Centers. *Chem. Rev.* **2005**, *105*, 1961–2002.
48. Langford, C. H.; Gray, H. B. *Ligand Substitution Processes*; Benjamin: New York, 1965.
49. Basolo, F.; Pearson, R. G. *The Mechanisms of Inorganic Reactions;* Wiley: New York, 1958.
50. MacMillan, S. N.; Lancaster, K. M. X-ray Spectroscopic Interrogation of Transition-Metal-Mediated Homogeneous Catalysis: Primer and Case Studies. *ACS Catal.* **2017**, *7*, 1776–1791.
51. Hummer, A. A.; Heffeter, P.; Berger, W.; Filipits, M.; Batchelor, D.; Buchel, G. E.; Jakupec, M. A.; Keppler, B. K.; Rompel, A. X-ray Absorption Near Edge Structure Spectroscopy to Resolve the in Vivo Chemistry of the Redox-Active Indazolium trans-[Tetrachlorobis(1H-indazole)ruthenate(III)] (KP1019) *J. Med. Chem.* **2013**, *56*, 1182–1196.
52. Langford, C. H.; Muir, W. H. Dissociative interchange mechanism for the formation of acidopentaamminecobalt(III) ions. *J. Am. Chem. Soc.* **1967**, *89*, 3141–3144.
53. Olmstead, W. N.; Bordwell, F. G. Ion-pair association constants in dimethyl sulfoxide. *J. Org. Chem.* **1980**, *45*, 3299–3305.
54. Functional: Chai, J.-D.; Head-Gordon, M. Long-range corrected hybrid density functionals with damped atom–atom dispersion corrections. *Phys. Chem. Chem. Phys.*, **2008**, *10*, 6615-6620. Basis set: Weigend, F.; Ahlrichs, R. Balanced basis sets of split valence, triple zeta valence and quadruple zeta valence quality for H to Rn: Design and assessment of accuracy. *Phys. Chem. Chem. Phys.*, **2005**, *7*, 3297-3305.
55. Bryndza, H. E.; Domaille, P. J.; Paciello, R. A.; Bercaw, J. E. Kinetics and mechanism of phosphine exchange for ruthenium(II) complexes in the series (.eta.5-C5Me5)(PMe3)2RuX. Ancillary ligand effects on dative ligand dissociation. *Organometallics* **1989**, *8*, 379–385.
56. Bryndza, H. E.; Domaille, P. J.; Tam, W.; Fong, L. K.; Paciello, R. A.; Bercaw, J. E. Comparison of metal-hydrogen, -oxygen, -nitrogen and -carbon bond strengths and evaluation of functional group additivity principles for organoruthenium and organoplatinum compounds. *Polyhedron*, **1988**, *7*, 1441-1452.
57. Dias, P. B.; Minas de Piedade, M. E.; Martinho Simoes, J. A. Bonding and energetics of phosphorus (III) ligands in transition metal complexes. *Coord. Chem. Rev.* **1994**, *135-136*, 737-807.
58. Abe, M.; Mitani, A.; Ohsawa, A.; Herai, M.; Tanaka, M.; Sasaki, Y. A kinetic study on pyridine exchange reactions at a bis(μ-acetato)(μ-oxo)diruthenium(III) center: effects of monodentate and bidentate N-heterocyclic ligands cis to the oxo bridge. *Inorg. Chim. Acta.* **2002**, *331*, 156-167.

59. Ido, Y.; Sakaguchi, K.; Tasei, M.; Minami, S.; Sawamoto, H.; Fujihara, T.; Nagasawa, A. A Kinetic Study on the Substitution for Acetonitrile at the trans -to-μ-Oxido Sites in a Bis(μ-acetato)(μ-oxido)diruthenium(III) Dipositive Complex: Dissociative–Associative Transition of the Activation Mode for the Substitution of Pyridine Derivatives. *Eur. J. Inorg. Chem.* **2013**, 3641-3650.
60. Ikeda, Y.; Tomiyasu, H.; Fukutomi, H. A Nuclear Magnetic Resonance Study of the Kinetics of Ligand Exchange Reactions in Uranyl Complexes. III. Dimethyl Sulfoxide Exchange in Bis(β-diketonato)(dimethyl sulfoxide)dioxouranium(VI). *Bull. Chem. Soc. Jpn.* **1983**, *56*, 1060-1066.
61. Crick, I. S.; Tregloan, P. A. Temperature and pressure dependent equilibrium studies of 1, 4, 8, 11-tetramethyl-1, 4, 8, 11-tetraazacyclotetradecane nickel(ii) in coordinating solvents. *Inorg. Chim. Acta.* **1988**, *142*, 291-299.
62. Bockris, J. O'M.; Reddy, A. K. N. *Modern Electrochemistry 1: Ionics, 2nd Ed.,* Kluwer Academic Publishers: New York, 2002.
63. Dissociative reactions nearly always have positive values for volume of activation: Asano, T.; Le Noble, W. J. Activation and reaction volumes in solution. *Chem. Rev.* **1978**, *78*, 407–489.
64. Though the density of charge carriers for the exact carbon black that we used (Monarch 1300) is not reported, we note that other carbon blacks of similar particle size and surface area are conductive: a) Liu, C.-C.; Walters, A. B.; Vanice, M. A. Measurement of electrical properties of a carbon black. *Carbon*, **1995**, *33*, 1699-1708. b) Khodabakhshi, S.; Fulvio, P. F.; Andreoli, F. Carbon black reborn: Structure and chemistry for renewable energy harnessing. *Carbon*, **2020**, *162*, 604-649. c) Kendall, K. Solid surface energy measured electrically. *J. Phys D: Appl. Phys.,* **1990**, *23*, 1329-1331.
65. Bockris, J. O'M.; Reddy, A. K. N.; Gamboa-Aldeco, M.*Modern Electrochemistry 2A: Fundamentals of Electrodics*, *2nd Ed.* Kluwer Academic Publishers: New York, 2002.

SYNOPSIS TOC (Word Style “SN_Synopsis_TOC”). If you are submitting your paper to a journal that requires a synopsis graphic and/or synopsis paragraph, see the Instructions for Authors on the journal’s homepage for a description of what needs to be provided and for the size requirements of the artwork.

Authors are required to submit a graphic entry for the Table of Contents (TOC) that, in conjunction with the manuscript title, should give the reader a representative idea of one of the following: A key structure, reaction, equation, concept, or theorem, etc., that is discussed in the manuscript. Consult the journal’s Instructions for Authors for TOC graphic specifications.